Materials Advances

ROYAL SOCIETY OF CHEMISTRY

PAPER

View Article Online
View Journal | View Issue

Cite this: *Mater. Adv.*, 2025, 6, 3889

Crystalline structure modification of hydroxyapatite *via* a hydrothermal method using different modifiers

Md. Kawsar,[ab] Md. Sahadat Hossain, *[a] Newaz Mohammed Bahadur,[b] Dipa Islam[c] and Samina Ahmed *[a]

Received 7th April 2025,
Accepted 19th April 2025

DOI: 10.1039/d5ma00334b

rsc.li/materials-advances

In this study, hydroxyapatite (HAp) was synthesized using the hydrothermal method, where different modifiers, such as succinic acid, ascorbic acid, stearic acid, calcium phosphate, and silica, were used. The powdered HAp's morphological, compositional, and crystallographic features were explored using Fourier-transform infrared spectroscopy (FTIR), field emission scanning electron microscopy (FESEM), and X-ray diffraction (XRD) characterization techniques. Crystallographic characteristics, such as the lattice parameter, unit cell volume, and crystallinity degree, were calculated by utilizing XRD data. The crystallite size (<100 nm) was calculated using various models, including the Scherrer equation, the Sahadat–Scherrer model, the size-strain plot, the Halder–Wagner model, and different forms of Williamson–Hall plot. Williamson–Hall includes the uniform deformation model (UDM), the uniform stress deformation model (USDM), and the uniform deformation energy density model (UDEDM). Some models incorporate energy density, strain, and stress as additional components. The peaks at 962, 1026, and 1087 and 3000–3800 cm^{-1} in FTIR absorption spectra indicated the presence of phosphate and hydroxide groups in the synthesized HAp. Additionally, the optical bandgap energy of the synthesized Hap was estimated to range from 5.29 eV to 5.60 eV. Rietveld refinement analysis revealed that HAp is the predominant phase, with tricalcium phosphate (TCP) generated alongside.

1 Introduction

More than 2.2 million individuals undergo surgical procedures to address severe bone abnormalities resulting from accidents, illnesses, and trauma.[1] The increased rate of surgery on human bone has led to relevant developments concerning synthetic biomaterials, which initially posed challenges due to infections caused by aseptic surgical techniques.[2] Bioactive calcium phosphate ceramics, particularly hydroxyapatite (HAp), are highly biocompatible owing to their crystallographic and chemical comparability with bone and tooth mineral constituents.[3] HAp bioceramics are known for their high level of biocompatibility and are commonly used for dense and porous bioceramic preparations. Owing to their low mechanical reliability in aqueous environments, they are unsuitable for heavy load-bearing applications. Instead, they are used as biocompatible phase reinforcements in composites, metal implant coatings, and human tissue incorporation.[4,5] Additionally, HAp can be used as a protein delivery agent, as a drug delivery agent, and in chromatography.[6] Numerous techniques have been listed for HAp synthesis, including hydrothermal,[7,8] hydrolysis,[9] combustion methods,[10] solid-state methods,[11] electrochemical deposition,[12] and wet chemical precipitation methods.[13] Frequent problems in synthesis methods include non-stoichiometric products, agglomeration, uncontrolled particle size, and long reaction times, highlighting the need for better morphological control.[10] The hydrothermal process is a chemical precipitation method used to prepare HAp through chemical reactions using water as the solvent at elevated pressure and temperatures, resulting in the aging process within a pressure vessel or an autoclave.[14] This process involves the transformation of liquids, gels, or slurries into crystalline phases under moderate conditions, producing needle-shaped powders with lengths between 100 and 160 nm and diameters between 20 and 40 nm.[4,14] In recent years, studies have shown that the dimensions and shapes of HAp can be regulated by altering the hydrothermal reaction temperature and time.[15] This method has led to the preparation of high-purity hydroxyapatite with various shapes, including spine-like, needle-like, rod-like, flake, nano-spherical, and hexagonal prisms.[10,16,17] Modifiers are used to modify the crystalline structure of HAp based on their unique chemical properties.[13,18,19] Succinic acid influences the

[a] *Glass Research Division, Institute of Glass & Ceramic Research and Testing, Bangladesh Council of Scientific and Industrial Research (BCSIR), Dhaka 1205, Bangladesh. E-mail: saz8455@gmail.com, shanta_samina@yahoo.com*
[b] *Department of Applied Chemistry and Chemical Engineering, Noakhali Science and Technology University, Noakhali, Bangladesh*
[c] *Bangladesh Toxicological Research Institute (BTRI), Bangladesh Council of Scientific and Industrial Research (BCSIR), Dhaka 1205, Bangladesh*

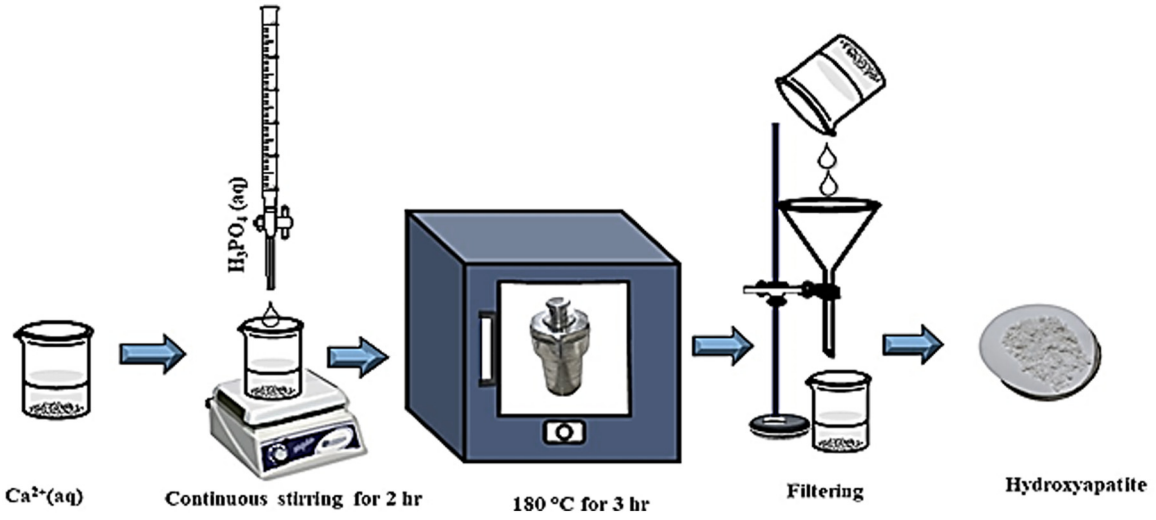

Fig. 1 Hydrothermal synthesis of hydroxyapatite.

growth and morphology of HAp crystals by interacting with calcium ions, thereby altering the crystallization process and affecting crystal size, shape, and surface properties.[20,21] Ascorbic acid stabilizes the HAp structure and introduces functional groups that enhance biological activity, improving biocompatibility and bioactivity for applications like bone regeneration.[22] Stearic acid acts as a surfactant, limiting growth and controlling particle size distribution, resulting in smaller, more uniform crystals with enhanced dispersibility.[21] Calcium phosphate maintains the balance between calcium and phosphate ions, ensuring pure HAp with controlled crystallinity and phase composition.[22] Silica is added to modify surface properties and improve mechanical strength, acting as a nucleation site for HAp crystal growth and enhancing bioactivity, osteoconductivity, and mechanical stability, making it suitable for bone tissue engineering.[23] Each modifier tailors the structural and functional properties of HAp for specific applications. In this study, various modifiers like succinic acid, ascorbic acid, stearic acid, calcium phosphate, and silica were used to modify the morphological features (*e.g.*, shape and size) of HAp *via* the hydrothermal method.

2 Experimental

2.1 Materials

$Ca(OH)_2$ and H_3PO_4 were used as the sources of Ca^{2+} and PO_4^{3-}, respectively. Additionally, several organic modifiers such as succinic acid ($C_4H_6O_4$), ascorbic acid ($C_6H_8O_6$), stearic acid ($C_{18}H_{36}O_2$), calcium phosphate ($Ca_3(PO_4)_2$), and silica (SiO_2) were purchased from E-Merck, Germany. In addition, to maintain the solution pH (10–11), HNO_3 and NH_4OH were used.

2.2 Methods

2.2.1 HAp synthesis *via* hydrothermal method. In this synthesis process, a precalculated amount of Ca^{2+} and PO_4^{3-} is dissolved in DI and continuously stirred for 2 h. Different organic modifiers like succinic acid ($C_4H_6O_4$), ascorbic acid ($C_6H_8O_6$), stearic acid ($C_{18}H_{36}O_2$), calcium phosphate ($Ca_3(PO_4)_2$), and silica (SiO_2) at the amount of 0.1 g were dissolved into the solution to modify the crystalline structure of the synthesized HAp. Subsequently, the solution was delivered to an autoclave reactor made of stainless steel containing PTFE and then heated at 180 °C for 3 h (Fig. 1). After cooling, the mixture was separated and rinsed with DI water. The precipitate (ppt) was subjected to a temperature-controlled oven process (105 °C), where it was dried for 3 h before being cooled and analyzed.

2.2.2 Characterization. A sophisticated XRD instrument (Rigaku Smart Lab) was used to analyze the crystallographic features of as-synthesized nanocrystalline HAp using an X-ray diffraction machine, with scanning steps of 0.01 and scanning range at 2θ = 20–60°. The Ni-Kβ filter was placed to minimize Kβ-rays, and the experiment was calibrated using standard silicon. The optical bandgap was determined using a UV-2900 spectrophotometer, and the FTIR study was conducted using an IR prestige 21 spectrometer. Morphological scans were acquired using a field emission scanning electron microscopy (FESEM) device (Schottky JSM-7610F, Japan) while an accelerating voltage of 10 kV was maintained to obtain the images.[24]

3 Results and discussion

3.1 Crystallographic characterization

Fig. 2 shows the XRD pattern of the synthesized HAp. According to the output data, the reflected peak positions in 2θ values, including the plane, were 25.931° (002), 31.831° (211), 32.241° (112), 32.961° (300), 34.121° (202), 39.881° (130), 46.751° (222), and 49.531° (213). The HAp profiles were matched using standard criteria (ICDD database (card no: # 01-074-0565)).

The "preferential growth" in XRD data is a fundamental parameter that directly affects the "crystallite structure".[20,25] The obtained XRD patterns revealed preferences, with the sample's relative intensity estimated using the (211) plane in comparison with planes (002), (202), and (300), using an

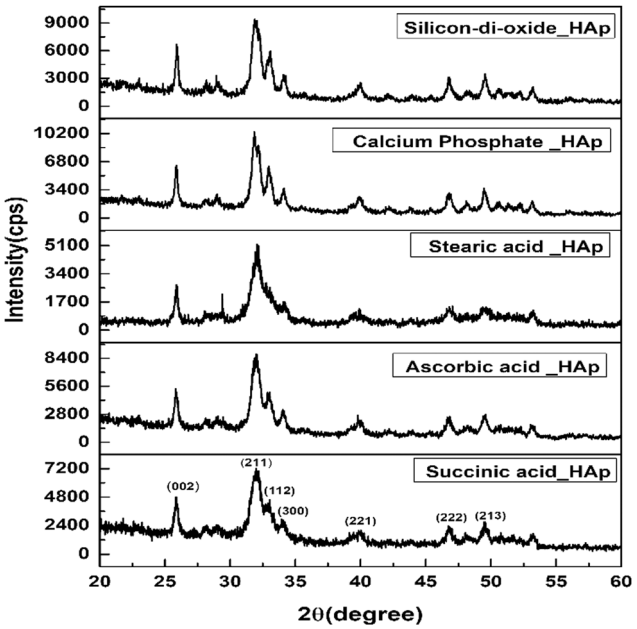

Fig. 2 XRD patterns of synthesized HAp using the Hydrothermal method.

equation to calculate RI.[26]

$$\text{Relative intensity, RI} = \frac{I_{(211)}}{I_{(002)} + I_{(202)} + I_{(300)}} \quad (1)$$

To deduce the relative intensity (RI) regarding the considered crystal plane, ICDD card's intensities were examined, and the preference growth of the HAp samples was determined using mathematical eqn (2), based on the measured RI of succinic acid_HAp, ascorbic acid_HAp, stearic acid_HAp, calcium phosphate_HAp, and silica_HAp (Table 1),[25]

$$\text{Preference growth, } P = \frac{\text{RI} - \text{RI}_s}{\text{RI}_S} \quad (2)$$

RI denotes the relative intensity of the plane, and RIs is the standard relative intensity of the plane. Table 1 lists the preference growth of (211) planes for succinic acid_HAp, ascorbic acid_HAp, stearic acid_HAp, calcium phosphate_HAp, and silica_HAp. The synthesized HAp exhibits preference growth, as indicated by negative magnitudes, which indicate higher preferences in specific planes. Positive magnitudes indicate an increased concentration of atoms in the corresponding plane due to specimen agglomeration, resulting in dimensional stability and minimal surface energy in crystallites.

Data analysis revealed various crystallographic characteristics, including lattice parameters, crystalline index, crystallite dimensions, unit cell volume, dislocation density, micro-strain, crystallinity degree, and specific surface area, which were calculated using eqn (3)–(9) and listed in Table 2.[27–29]

$$\text{Lattice parameter equation, } \left(\frac{1}{d_{hkl}}\right)^2 = \frac{4}{3}\left(\frac{h^2 + hk + k^2}{a^2}\right) + \frac{l^2}{c^2} \quad (3)$$

$$\text{Crystallinity index, } \text{CI}_{\text{XRD}} = \sum \frac{\mathbf{H}_{(202)} + \mathbf{H}_{(300)} + \mathbf{H}_{(112)}}{\mathbf{H}_{(211)}} \quad (4)$$

$$\text{Crystalline dimension, } D_c = k\lambda/\beta\cos\theta \quad (5)$$

$$\text{Cell volume: } V = \frac{\sqrt{3}}{2}a^2c \quad (6)$$

Table 1 Relative intensities and preference growth of HAp

Synthesized HAp from	Considered plane	Intensities of the plane	The relative intensity of the sample	Standard relative intensity	Preferential growth
Succinic acid_HAp	002	21.27	0.13	0.18	−0.86
	211	100	1.17	0.84	0.17
	202	0	0	0.1	−1
	300	63.48	0.52	0.39	−0.47
Ascorbic acid_HAp	002	28.09	0.13	0.18	−0.86
	211	91.97	0.63	0.84	−0.36
	202	15.82	0.24	0.1	−0.75
	300	100	0.73	0.39	−0.26
Stearic acid _HAp	002	2.39	0.023	0.18	−0.97
	211	100	41.84	0.84	4.84
	202	0	0	0.1	−1
	300	0	0	0.39	−1
Calcium phosphate_HAp	002	5.7	0.14	0.18	−0.85
	211	26.74	1.4	0.84	0.47
	202	3.61	0.08	0.1	−0.91
	300	8.79	0.24	0.39	−0.75
Silica_HAp	002	20.81	0.14	0.18	−0.85
	211	100	1.54	0.84	0.54
	202	12.65	0.08	0.1	−0.91
	300	31.21	0.23	0.39	−0.76

Table 2 Hydrothermally synthesized hydroxyapatite crystallographic variables

Parameter	Succinic acid_HAp	Ascorbic acid_HAp	Stearic acid_HAp	Calcium phosphate_HAp	Silica_HAp
Lattice parameter $a = b$ (Å)	9.38 ± 0.02	9.42 ± 0.01	9.39 ± 0.02	9.42 ± 0.01	9.45 ± 0.01
Lattice parameter c (Å)	6.88 ± 0.01	6.90 ± 0.01	6.86 ± 0.01	6.88 ± 0.01	6.87 ± 0.01
Crystal size, D_c (nm)	8.69 ± 0.5	33.51 ± 1.2	55.13 ± 2.0	63.62 ± 2.5	76.47 ± 3.0
Unit cell volume, V (Å^3)	524.53 ± 1.5	530.25 ± 1.2	523.82 ± 1.3	529.36 ± 1.1	513.31 ± 1.0
Degree of crystallinity, X_c	(16.1 ± 0.5) × 10^{-3}	1.49 ± 0.05	4.096 ± 0.1	6.30 ± 0.2	10.97 ± 0.3
Microstrain, ε (×10^{-3})	14.58 ± 0.2	10.42 ± 0.1	2.27 ± 0.05	1.98 ± 0.05	1.65 ± 0.05
Dislocation density, δ (×10^{15} lines per m^2)	13.22 ± 0.5	0.89 ± 0.05	0.3289 ± 0.01	0.246 ± 0.01	0.17 ± 0.01
Crystallinity index, CI_XRD	1.85 ± 0.05	2.13 ± 0.05	1.25 ± 0.05	1.64 ± 0.05	1.88 ± 0.05
Specific surface area, S (m^2 g^{-1})	0.21 ± 0.01	0.056 ± 0.005	0.034 ± 0.003	0.029 ± 0.002	0.024 ± 0.002

$$\text{Dislocation density: } \delta = \frac{1}{(D_c)^2} \tag{7}$$

$$\text{Microstrain: } \varepsilon = \beta/4\tan\theta \tag{8}$$

$$\text{Degree of crystallinity: } X_c = \left(\frac{K_a}{\beta}\right)^3 = \left(\frac{0.24}{\beta}\right)^3 \tag{9}$$

$$\text{Specific surface area: } s = \frac{6}{\rho \times D_c}\ \text{m}^2\ \text{g}^{-1} \tag{10}$$

The plane (h,k,l) identifies specific unit cells, and lattice parameters are expressed by a, b, c, and the crystallinity degree is denoted as X_c.[30] δ, $H_{(hkl)}$, and CI_{XRD} are used to measure dislocation density, peak height, and the crystalline index of synthesized HAp. Eqn (8) was used to compute the specific surface area, representing D_c (crystallite size) and ρ (density) (3.16 g cm^{-3}), respectively.[31] The crystallographic variables associated with hydrothermally synthesized HAp significantly influence the structural characteristics of the material. The lattice parameters (a, b, c) remained relatively consistent across all samples, confirming the upholding of the hexagonal crystal structure, although silica incorporation slightly expanded the unit cell. Crystal size varies notably, with succinic acid_HAp exhibiting the smallest (8.69 nm) and silica_HAp having the largest (76.47 nm), indicating that inorganic modifiers promote larger crystals, while organic modifiers hinder growth. The unit cell volume follows a similar trend, with silica_HAp having the smallest volume, suggesting a denser lattice structure. The degree of crystallinity is highest for silica_HAp (10.97) and lowest for succinic acid_HAp, demonstrating that inorganic modifiers enhance crystallinity, whereas organic modifiers disrupt it. Microstrain, an indicator of lattice distortion, is highest in succinic acid_HAp (14.58 × 10^{-3}) and lowest in silica_HAp, indicating that organic modifiers induce more internal stress. The dislocation density, which reflects structural defects, is also highest for succinic acid_HAp and lowest for silica_HAp, supporting the observation that inorganic modifiers contribute to more stable defect-free crystals. The crystallinity index (CIXRD) indicates that ascorbic acid_HAp has the most well-ordered structure, whereas stearic acid_HAp exhibits the lowest crystallinity. Additionally, the specific surface area is highest for succinic acid_HAp and lowest for silica_HAp, correlating with crystal size and defect density. Overall, inorganic modifiers like silica and calcium phosphate promote larger crystal growth, higher crystallinity, and lower defect densities, leading to more stable HAp structures, whereas organic modifiers like succinic acid and stearic acid result in smaller crystals, lower crystallinity, and increased lattice strain. The preferred orientation of a polycrystalline material is determined by its texture coefficient, which is determined by its X-ray diffraction pattern and influences its crystallographic planes.[32] The value of the texture coefficient (TC) was estimated by fixing a distinct peak in the measured sample, and the peak in reference offers vital insights into the crystallographic orientation of a material, which significantly influences its performance in many applications.[33] The texture coefficient of the synthesized HAp can be calculated using eqn (11)

$$TC_{hkl} = \frac{I_{(hkl)}/I_{0(hkl)}}{\frac{1}{n}\sum_{1}^{N}\frac{I_{(hkl)}}{I_{0(hkl)}}} \tag{11}$$

The term $I_{(hkl)}/I_{0(hkl)}$ indicates the ratio of the relative intensity (RI) of the sample to the standard and $\frac{1}{n}\sum_{1}^{N}\frac{I_{(hkl)}}{I_{0(hkl)}}$ denotes the mean RI. The analysis reveals that succinic acid_HAp, ascorbic acid_HAp, calcium phosphate_HAp, and silica_HAp are grown in (002), (112), and (202) planes, while stearic acid_HAp is grown in (002) and (202) planes, respectively.

3.2 Crystal size estimation

3.2.1 Scherrer equation. The Scherrer equation is the first method to link the dimension of nano-crystallites with the broadening of peaks.[34,35] Eqn (3) proposes a mathematical expression for spherical crystallite, ignoring instrumental broadening and crystal defects, using parameters such as crystallite size (D_c), Scherrer constant (K), X-ray source's wavelength (λ), the full width at half maxima (β), and Bragg's angle (θ). On average, the crystal dimensions of the synthesized HAp were 11.51, 16.11, 29.65, 23.25, and 25.12 nm for succinic acid_HAp, ascorbic acid_HAp, stearic acid_HAp, calcium phosphate_HAp and silica_Hap, respectively.

3.2.2 Williamson–Hall method. The Scherrer method, widely used for calculating crystallite size, has limitations in determining grain boundary triple junctions, stacking faults, and the intrinsic strain of point defects.[36,37] Hence, the Williamsons–Hall method (W–H) and its revised version have been used, considering the inherent strain and particle size.[38,39] The crystallite size and microstrain significantly influence the physical streak widening of the peak of X-ray diffraction, leading to a total broadening.

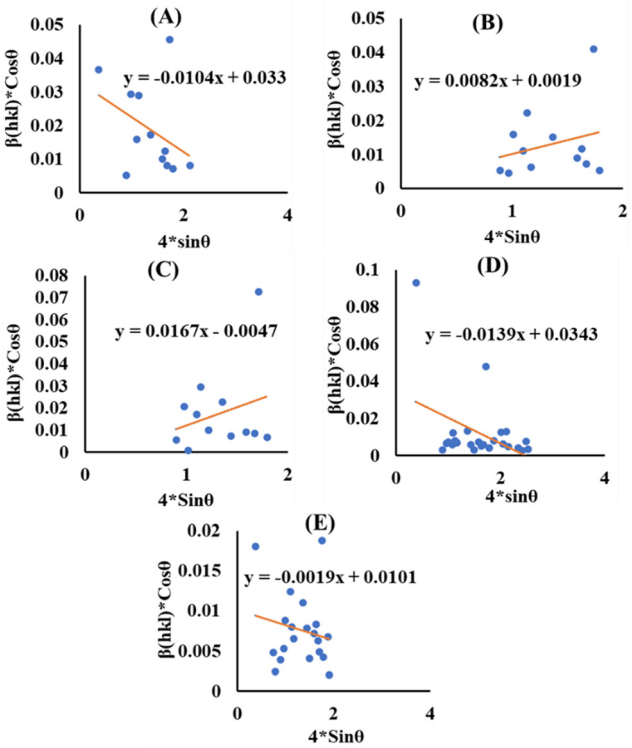

Fig. 3 UDM for (A) succinic acid_Hap, (B) ascorbic acid_Hap, (C) stearic acid_HAp, (D) calcium phosphate_HAp and (E) silica_HAp.

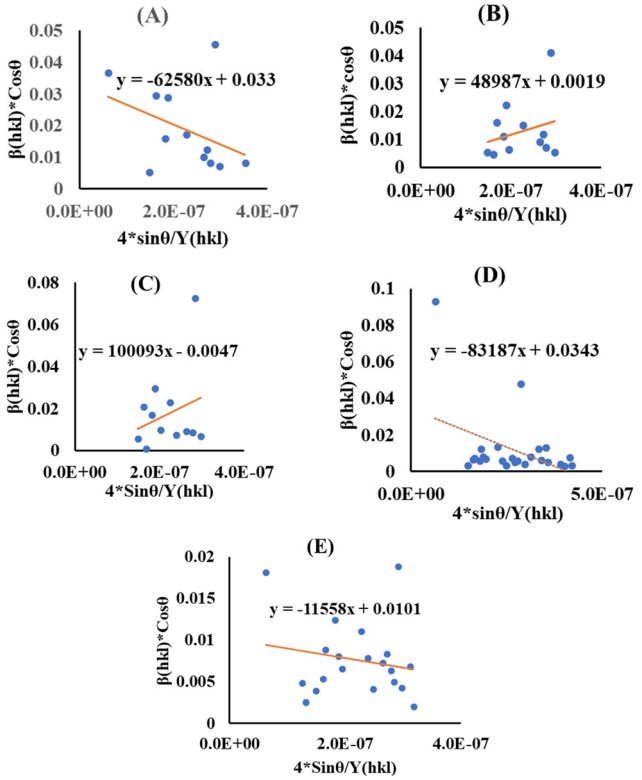

Fig. 4 USDM for (A) succinic acid_HAp, (B) ascorbic acid_HAp, (C) stearic acid _HAp, (D) calcium phosphate_HAp and (E) silica_HAp.

$$\beta_{\text{total}} = \beta_{hkl} + \beta_{\text{strain}} \tag{12}$$

This study used revised W–H equations (*e.g.*, UDM, USDM, and UEDM) to calculate crystallite dimension and microstrain, which are extensively mentioned in the subsequent segments.

3.2.3 Uniform deformation model (UDM). The UDM technique accounts for consistent deformation in nanocrystals caused by flaws in their crystal structure, leading to uniform strain in all directions.[40] The XRD profile's physical broadening due to intrinsic strain (β_{strain}) was considered,

$$\beta_{\text{strain}} = 4\varepsilon\cdot\tan\theta \tag{13}$$

where θ is the Bragg position. Rearranging eqn (5) and (13) yields...

$$\beta_{\text{total}} = \frac{K_{\text{B}}\lambda}{D_{\text{w}}\cos} + 4\cdot\varepsilon\cdot\tan(\theta) \tag{14}$$

$$\beta_{\text{total}}\cos = \frac{K_{\text{B}}\lambda}{D_{\text{w}}} + 4\varepsilon\sin\theta \tag{15}$$

Fig. 3 shows the plot of eqn (15), with terms ($4\sin\theta$) on the horizontal axis and ($\beta_{hkl}\times\cos\theta$) across the vertical axis, which assembles the obtained diffraction peaks for the HAp nanocrystals. Intrinsic strain for the crystal samples is provided *via* the slope of the as-generated linear graph, and the average size of the nanocrystal is estimated from the intercept. The lattice strain in nanocrystals originates from the expansion or contraction of the lattice, resulting in confinement to a small size. This alteration causes a small deviation in the atomic configuration compared to bulk crystals. Furthermore, the size constraint leads to imperfections in the lattice arrangement, causing strain inside the lattice. The average crystal size of the HAp is estimated as 4.20, 72.97, 29.50, 4.04, and 13.72 nm for succinic acid_HAp, ascorbic acid_HAp, stearic acid_HAp, calcium phosphate_HAp and silica_HAp, respectively.

3.2.4 Uniform stress deformation model (USDM). In the UDM, the specimen is assumed to be isotropic, although this assumption is not valid for real crystals. The Williamson–Hall equation was modified to incorporate an anisotropic factor to account for anisotropic crystals, creating the USDM.[41] Hooke's law holds that strain and stress are linearly connected, with stress represented as

$$\sigma = \varepsilon \times Y_{hkl} \tag{16}$$

Y_{hkl}, also known as Young's modulus, is a crucial factor in determining the strain of a material. Applying the strain value in eqn (15) and with modification, we obtain

$$\beta_{\text{total}}\cos\theta = \frac{K_{\text{B}}\lambda}{D_{\text{w}}} + 4\sigma\frac{\sin\theta}{Y_{hkl}} \tag{17}$$

The modified W–H model (eqn (17)), specifically the USDM, incorporates uniform stress along each crystallographic plane in the XRD pattern for HAp nanoparticles. The term ($4\sin\theta/Y_{hkl}$) on the horizontal and ($\beta_{hkl}\cos\theta$) on the vertical axis (Fig. 4) correspond to each peak in the XRD pattern. The slope represents the stress value, whereas the intercept shows the average crystallite size (Table 3).

Table 3 Estimated microstructural features of HAp

Model name		Crystallite dimension (nm), stress (N m^{-2}), energy density (J m^{-3})				
		Succinic acid_HAp	Ascorbic acid_HAp	Stearic acid _HAp	Calcium phosphate_HAp	Silica_HAp
Scherrer's equation		D_L = 11.51	16.11	29.65	23.24	25.12
Williamson–Hall method	UDM	ε = 0.0104	ε = 0.0082	ε = 0.0167	ε = 0.0139	ε = 0.0019
		D_w = 4.201	D_w = 72.97	D_w = 29.50	D_w = 4.04	D_w = 13.72
	USDM	σ = −62 580	σ = 48 987	σ = 100 093	σ = −83 187	σ = −11 558
		D_w = 4.20	D_w = 72.97	D_w = 29.50	D_w= 4.04	D_w= 13.72
	UDEM	u = 326.344	u = 199.96	u = 864.86	u = 6.4 × 10^{-11}	u = 11.13
		D_w = 4.20	D_w= 72.97	D_w = 29.50	D_w =4.04	D_w = 13.72
Size-strain plot, D_w		3.75	4.88	2.87	0.148	7.53
Halder–Wagner method, D_w		32.15	3.53	2.08	1.84	7.40
Sahadat–Scherrer model, D_{s-s}		15.93	20.6	138.6	29.50	33.81

3.2.5 Uniform deformation energy density model (UDEDM). The Williamson–Hall model was modified to account for real crystal defects by introducing the term energy density for estimating crystallite size and stress, known as the UDEDM. Hook's law, represented by eqn (18), describes the energy density.[37,42]

$$u = \varepsilon^2 \frac{Y_{hkl}}{2} \tag{18}$$

$$\beta_{total} \cos\theta = \frac{K_B \lambda}{D_w} + 4 \sin\theta \sqrt{u} \frac{\sqrt{2}}{\sqrt{Y_{hkl}}} \tag{19}$$

Eqn (19) was developed by a systematic modification of eqn (15), where the strain is integrated with the energy density, also known as UDEDM.[43] The plot of the eqn (19) reveals the energy density value of crystalline HAp nanoparticles, with components $(4 \sin\theta(\sqrt{2u/Y_{hkl}}))$ plotted horizontally and $(\beta_{hkl} \cdot \cos\theta)$ plotted vertically (Fig. 5), resembling each diffraction peak. All the estimated values of crystal size and energy density of the synthesized HAp nanoparticles are listed in Table 3.

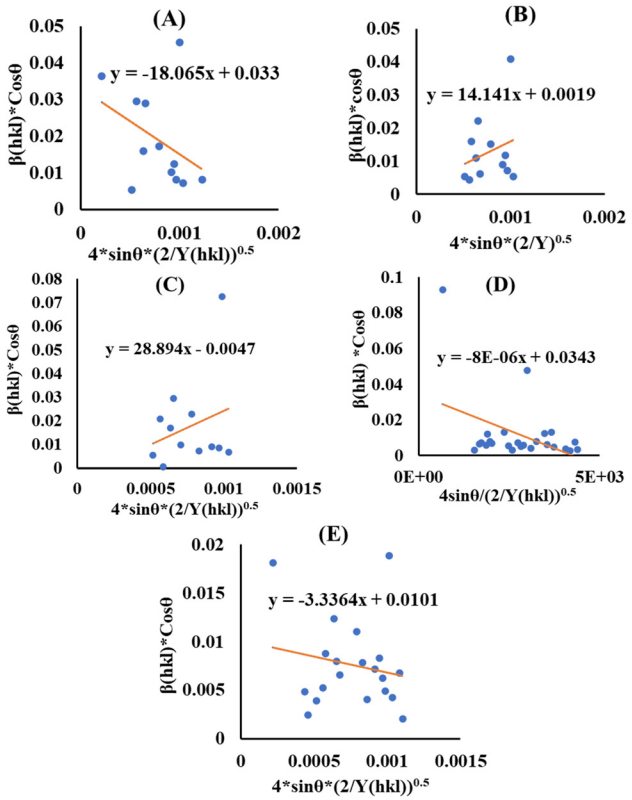

Fig. 5 UDEDM for (A) succinic acid_HAp, (B) ascorbic acid_HAp, (C) stearic acid _HAp, (D) calcium phosphate_HAp and (E) silica_HAp.

3.2.6 Size-strain plot method (SSPM). The SSPM, using both the Gaussian function (β_G) and Lorentzian function (β_L), effectively determines the size and strain of nano-crystallites in anisotropic crystal structures, as illustrated in eqn (20)[44]

$$\beta_{total} = \beta_L + \beta_G \tag{20}$$

The SSPM is particularly useful because it analyzes lower angles, and it is ordinarily expressed as shown in eqn (21).[45]

$$(d_{hkl}\beta_{hkl} \cos\theta)^2 = \frac{K_B \lambda}{D_w}(d_{hkl}{}^2 \beta_{hkl} \cos\theta) + \frac{\varepsilon^2}{4} \tag{21}$$

By illustrating $(d_{hkl}\beta_{hkl} \cos\theta)^2$ and $(d_{hkl}{}^2\beta_{hkl} \cos\theta)$ along the Y and X axes, respectively, several mathematical expressions were generated, as shown in Fig. 6. These expressions were then fitted to the equation of a straight line. The slopes of these equations were used to calculate the crystallite size, whereas the intercept yields the value of strain. The estimated sizes of the nano-crystallites are listed in Table 3.

3.2.7 Halder–Wagner method (HWM). The SSP method perceives strain widening as a Gaussian function, whereas size widening is considered a Lorentzian function. The XRD peak is not subject to either of these two functions because its peak area approaches the Gaussian function, yet its tail quickly declines.[46] The Halder–Wagner approach is used to address the issue of peak widening, assuming that it is a symmetric Voigt function, which can be denoted by eqn (22).[47,48]

$$\beta_{hkl}{}^2 = \beta_G{}^2 + \beta_L \beta_{hkl} \tag{22}$$

Here, β_G, β_L = FWHM of the Gaussian and Lorentzian functions.

$$\left(\frac{*\beta_{hkl}}{*d_{hkl}}\right)^2 = \frac{1}{D_w}\left(\frac{*\beta_{hkl}}{*d_{hkl}{}^2}\right)^{\bullet} + \left(\frac{\varepsilon}{2}\right)^2 \tag{23}$$

Here, $*\beta^{\bullet}_{hkl} = \frac{\beta_{hkl} \cos(\theta)}{\lambda}$ and $*d^{\bullet}_{hkl} = \frac{2d_{hkl} \sin(\theta)}{\lambda}$ the crystal size was estimated from the slope $(1/D_w)$ by plotting $(*\beta_{hkl}/*d_{hkl})^2$ and $(*\beta_{hkl}/*d_{hkl})^2$ on the vertical and horizontal axes, respectively, as shown in Fig. 7.

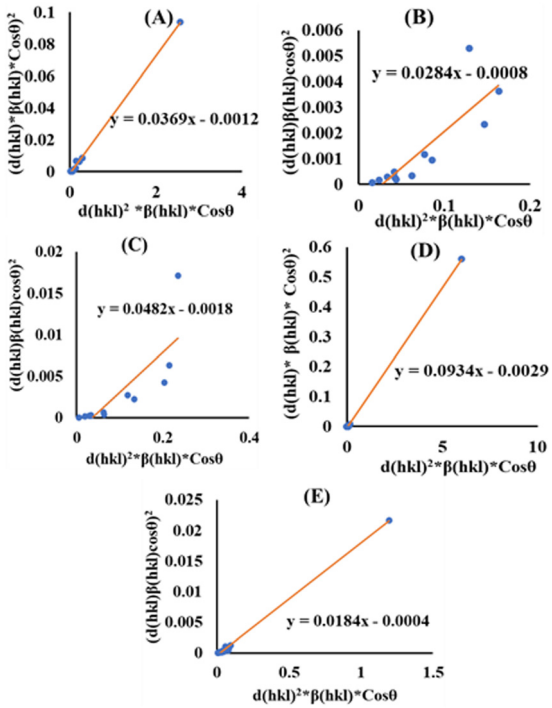

Fig. 6 SSPM for (A) succinic acid_HAp, (B) ascorbic acid_HAp, (C) stearic acid _HAp, (D) calcium phosphate_HAp and (E) silica_HAp.

3.2.8 Sahadat–Scherrer model (SSM). This model considers instrumental broadening and neglects intrinsic strain based on the Scherrer equation. It constructs a linear streak that passes through the (0,0) coordinate (origin), thereby allowing precise estimation of the crystallite dimension. Using this model, a varying range of crystal sizes can be calculated.[24,49] The model's formula can be expressed in eqn (24).

$$\cos\theta = \frac{K\lambda}{D_{S-S}} \times \frac{1}{\mathrm{FWHM}} \quad (24)$$

A straight line was constructed by scheming cos(θ) and 1/FWHM across the vertical and horizontal axes, with an additional line that precedes piercing the origin (Fig. 8). The aforementioned model can be used to deduce the sizes of HAp crystallites using the slope. Table 3 presents the measured crystalline dimensions of the synthesized HAp.

3.2.9 Critical analysis of crystallite size calculation methods and the effect of modifiers. The discrepancies observed among the crystallite size calculation methods arise from fundamental differences in their assumptions and limitations. The Scherrer equation[50,51] estimates size solely from peak broadening, ignoring lattice strain contributions, leading to overestimations in materials with significant defects or microstrains.[13] Modified approaches like the Williamson–Hall (W–H) methods separate size and strain effects by assuming uniform deformation (UDM), stress (USDM), or energy density (UDEDM), but these oversimplify strain heterogeneity in real systems.[13] The Sahadat–Scherrer model attempts to address linearity issues in earlier Scherrer-derived methods by enforcing origin-passing plots, yet its validity depends on idealized

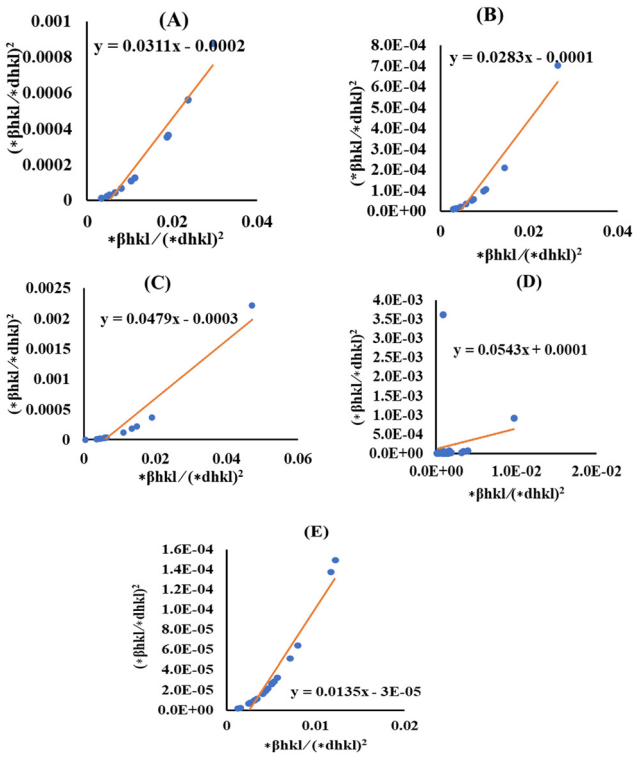

Fig. 7 HWM for (A) succinic acid_HAp, (B) ascorbic acid_HAp, (C) stearic acid _HAp, (D) calcium phosphate_HAp and (E) silica_HAp.

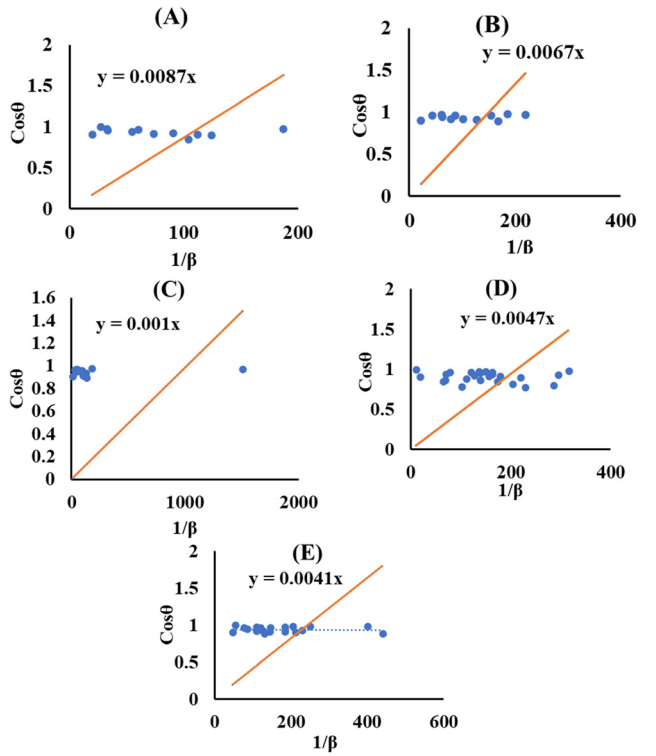

Fig. 8 SSM for (A) succinic acid_HAp, (B) ascorbic acid_HAp, (C) stearic acid_HAp, (D) calcium phosphate_HAp and (E) silica_HAp.

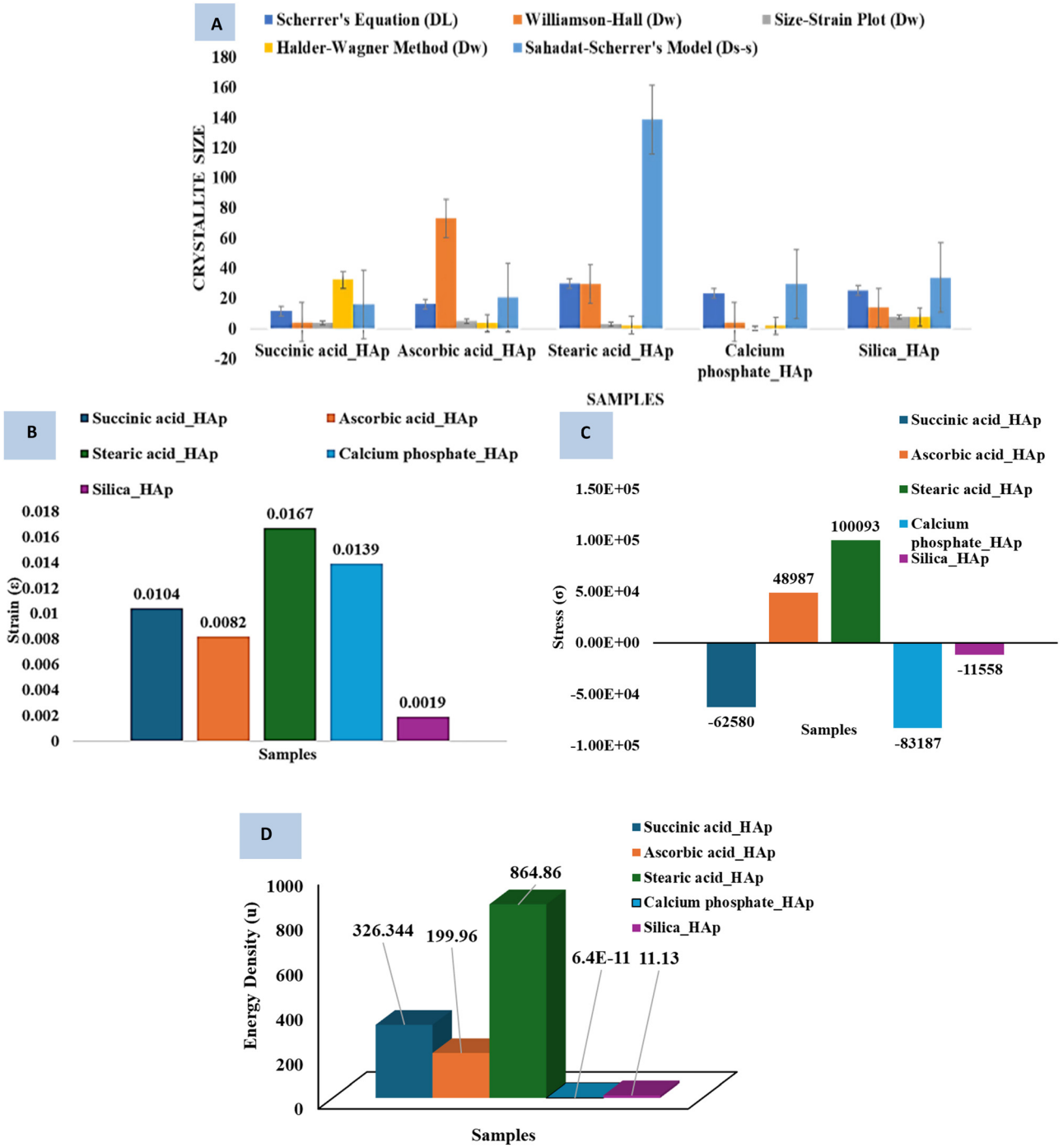

Fig. 9 Systematic comparison among (A) the crystallite size, (B) strain, (C) stress and (D) energy density.

peak broadening behavior, which is rarely observed experimentally.[49] Critically, instrumental broadening corrections introduce variability, as improper β_{hkl} adjustments propagate errors across all methods. Furthermore, crystallite shape anisotropy[52] and size-distribution effects differentially impact models—Scherrer assumes spherical crystals, whereas W–H methods require multiple diffraction peaks for reliable strain deconvolution.[13,20] The Halder–Wagner and size-strain plot methods improve the accuracy of nano-crystallites but struggle with sub-10 nm systems where surface defects dominate.[52] Ultimately, method selection must consider the dominant broadening mechanism (size *vs.* strain), crystallite morphology, and instrumental resolution because no universal model accounts for all material-specific variables.[49]

3.2.10 Systematic comparison of modifiers on HAp properties for practical applications. Stearic acid HAp has the most significant impact on HAp properties, with the largest crystallite size (138.6 nm), highest strain (0.0167), substantial tensile

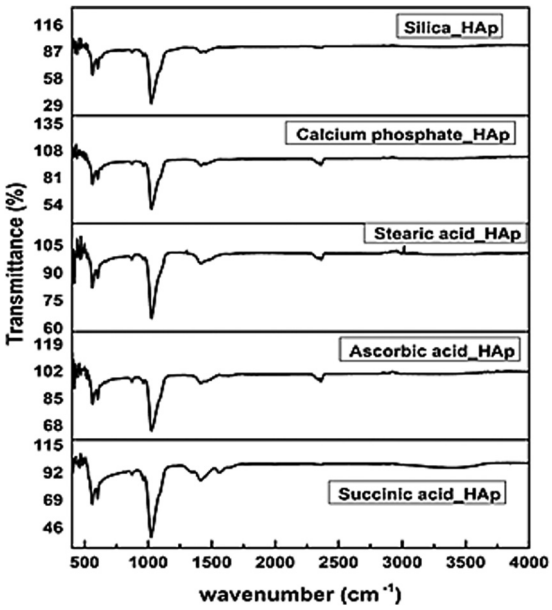

Fig. 10 Functional group analysis of hydrothermally synthesized HAp.

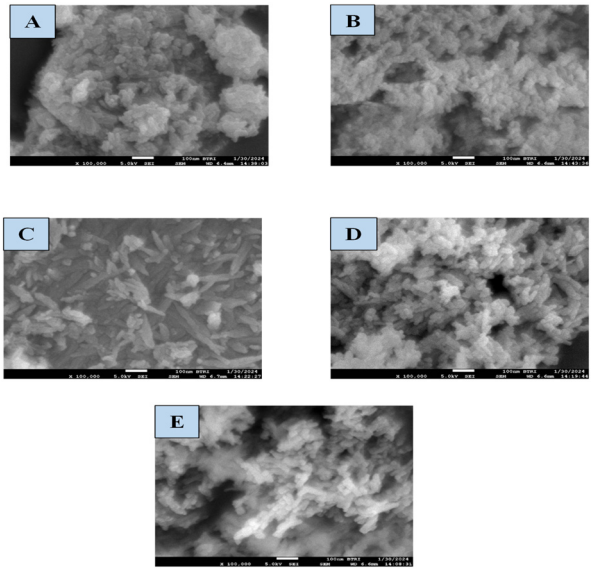

Fig. 11 SEM images of hydrothermally synthesized (A) succinic acid_HAp, (B) ascorbic acid_HAp, (C) stearic acid _HAp, (D) calcium phosphate_HAp and (E) silica_HAp.

stress (100 093 N m^{-2}), and highest energy density (864.86 J m^{-3}) (Fig. 9). This makes it a strong candidate for high-stress applications requiring energy absorption, such as impact-resistant coatings and energy storage materials. Calcium phosphate HAp has the smallest crystallite size (0.148 nm) and negligible energy density (6.4×10^{-11} J m^{-3}), but it induces high compressive stress (−83 187 N m^{-2}), limiting its practical utility. Succinic acid HAp has a moderate crystallite size (11.51 nm) and strain (0.0104), making it suitable for bioactive applications like bone implants and drug delivery systems.[53] Ascorbic acid HAp has balanced properties, with a crystallite size of 16.11 nm, moderate tensile stress (48 987 N m^{-2}), and stable energy density (199.96 J m^{-3}), suggesting its potential for applications requiring both structural integrity and functional performance. Silica HAp exhibits minimal strain (0.0019) and low energy density (11.13 J m^{-3}), making it suitable for stable, low-stress applications.

3.2.11 Functional group analysis. The FTIR spectroscopy of hydrothermally generated hydroxyapatite (HAp) revealed characteristic peaks connected to the optically active groups, particularly PO_4^{3-} and OH^-. The peaks include ν_1 oscillation at 962 cm^{-1}, ν_3 vibrations at 1026 and 1087 cm^{-1}, ν_4 bending at 563 and 599 cm^{-1}, and ν_2 bending at 473 cm^{-1}. Peaks within the 3000–3800 cm^{-1} range indicate the occurrence of OH^- groups.[20,54–56] Silica-HAp spectra do not display separate Si–O–Si peaks in the 1000–1200 cm^{-1} region due to interference from a strong phosphate band (Fig. 10).[57] The calcium phosphate-HAp control sample exhibited more identifiable spectrum features, suggesting negligible organic change. Stearic acid-HAp revealed a modest band at 2850–2960 cm^{-1}, suggesting C–H stretching vibrations from the alkyl chain.[58] The spectra of ascorbic acid-HAp validated the presence of HAp but did not reveal distinct peaks for ascorbic acid. Succinic acid-HAp spectra also indicated HAp without unequivocal evidence of the modifier. The peak near 2350 cm^{-1} was due to environmental carbon dioxide.[20] Overall, the resolution of the spectra appears limited, likely due to the presence of functional groups from the modifiers and low concentrations, which hinder the definitive identification of the modifiers.

3.2.12 Surface morphology study. The scanning electron microscopic technique (SEM) images (Fig. 11) of hydrothermally synthesized HAp exhibit distinct morphological characteristics. Succinic acid_HAp has an aggregated, cluster-like structure with densely packed irregular particles, indicating an enhanced surface area and improved bioactivity.[53] Ascorbic acid_HAp has a fluffy, cloud-like texture, suggesting reduced particle agglomeration and improved dispersibility. Stearic acid_HAp has a well-defined rod-like or needle-like structure, promoting its mechanical stability. Calcium phosphate_HAp has a porous, sponge-like structure with visible voids, enhancing osteoconductivity and biointegration.[59] Silica_HAp has a flaky, sheet-like texture with layered formations, which are linked to improved thermal stability and controlled drug delivery applications.[60] These variations in morphology highlight the influence of organic acids and synthesis conditions on HAp's structural characteristics, which are crucial for different applications.

3.3 Assessment of optical properties

The optical bandgap is a fundamental parameter representing the required energy for a single electron to pass from the valence band to the conduction band. This energy was computed using Tauc plots, as expressed by eqn (25) (Fig. 12).[61,62]

$$\alpha h\vartheta = A(h\vartheta - E_g)^n \quad (25)$$

The formula comprises α as the absorption factor, $h\vartheta$ as the photon energy, A as a constant value, and n as either a 2 (indirect) or $\frac{1}{2}$ (direct) permitted band gap. The band gaps of

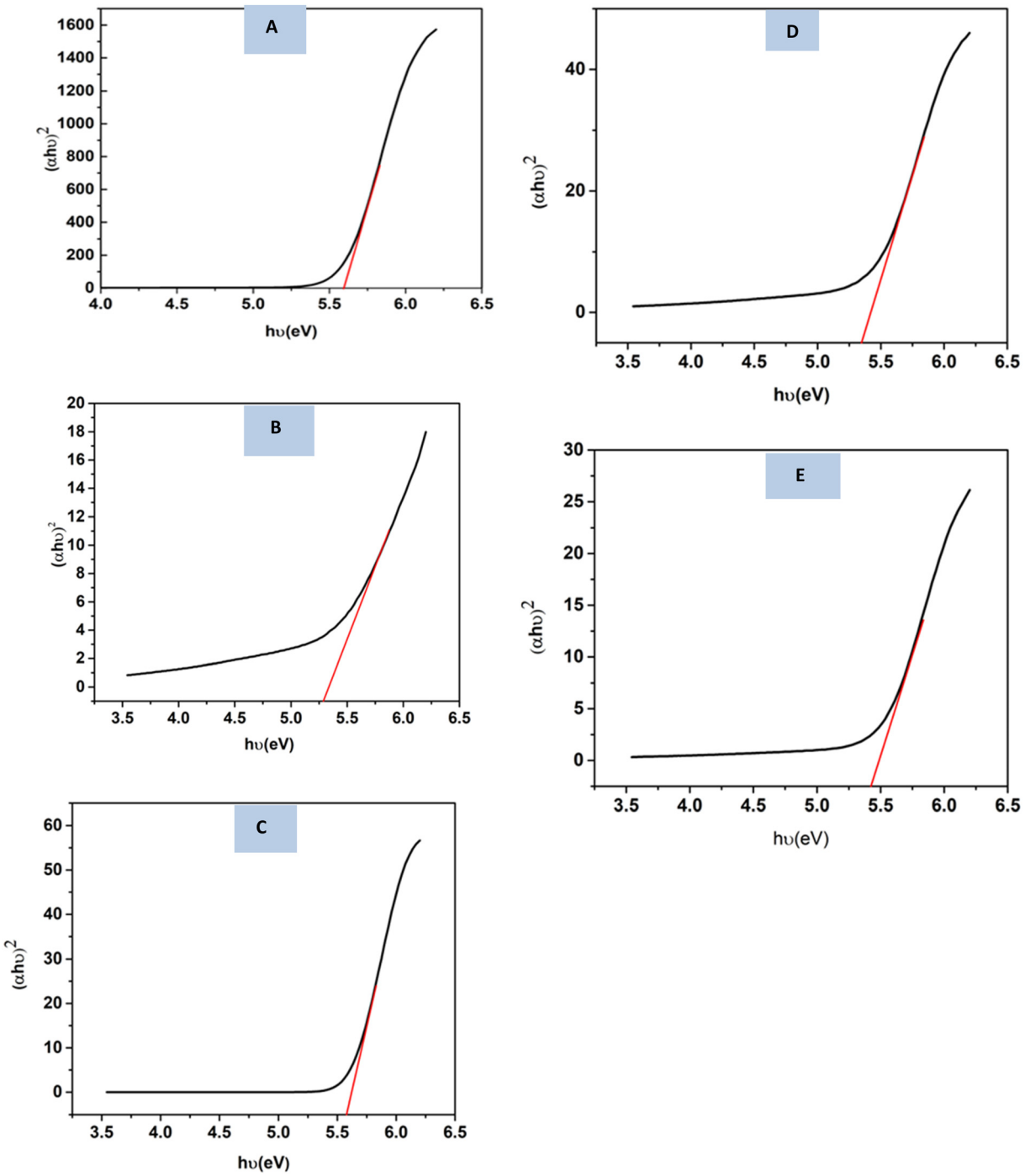

Fig. 12 Optical band gap estimation for (A) succinic acid_HAp, (B) ascorbic acid_HAp, (C) stearic acid _HAp, (D) calcium phosphate_HAp and (E) silica_HAp.

the HAp specimens are listed in Table 4. The literature reveals a link between crystallite size and optical band gap energy, with bigger crystallites lowering the optical band gap and *vice versa*.[63]

3.4 Quantitative analysis of the XRD data

The Rietveld refinement data confirmed the key conclusions of the synthesized HAp samples (Fig. 13).

Calcium phosphate_HAp and silica_HAp exhibit superior phase purity with 94.7% and 94% HAp content, respectively, with low R_{wp} values. However, their low χ^2 suggests potential over-parameterization in the refinement model. Stearic acid_-HAp exhibited the poorest performance, with only 84.2% HAp and 15.8% TCP and the highest R_{wp}, indicating significant refinement challenges due to sample heterogeneity. Ascorbic and succinic acid_HAp exhibited moderate purity with

Table 4 Measured band gaps of the synthesized HAp

Samples	Band gap (eV)
Succinic acid_HAp	5.60
Ascorbic acid_HAp	5.29
Stearic acid_HAp	5.57
Calcium phosphate_HAp	5.35
Silica_Hap	5.42

Table 5 Different phase estimation *via* the Rietveld refinement method

Samples	HAp phase (%)	TCP phase (%)	R_{wp}	R_{exp}	χ^2	GoF
Succinic acid_HAp	88.2	11.2	15.05	16.60	0.8220	0.9066
Ascorbic acid_HAp	92.5	7.5	16.00	17.05	0.8806	0.9384
Stearic acid_HAp	84.2	15.8	26.71	27.82	0.9218	0.9601
Calcium phosphate_HAp	94.7	5.3	15.26	19.11	0.6377	0.7985
Silica_HAp	94	6	14.63	16.96	0.7441	0.8626

acceptable refinement metrics (Table 5). Silica_HAp shows the most balanced refinement. The results highlight the critical relationship between synthesis conditions and refinement outcomes, with inorganic modifiers producing more phase-pure HAp with superior refinement characteristics. Organic acids, particularly stearic acid, introduce greater TCP impurities and compromise refinement quality, emphasizing the importance of modifier selection in HAp synthesis.

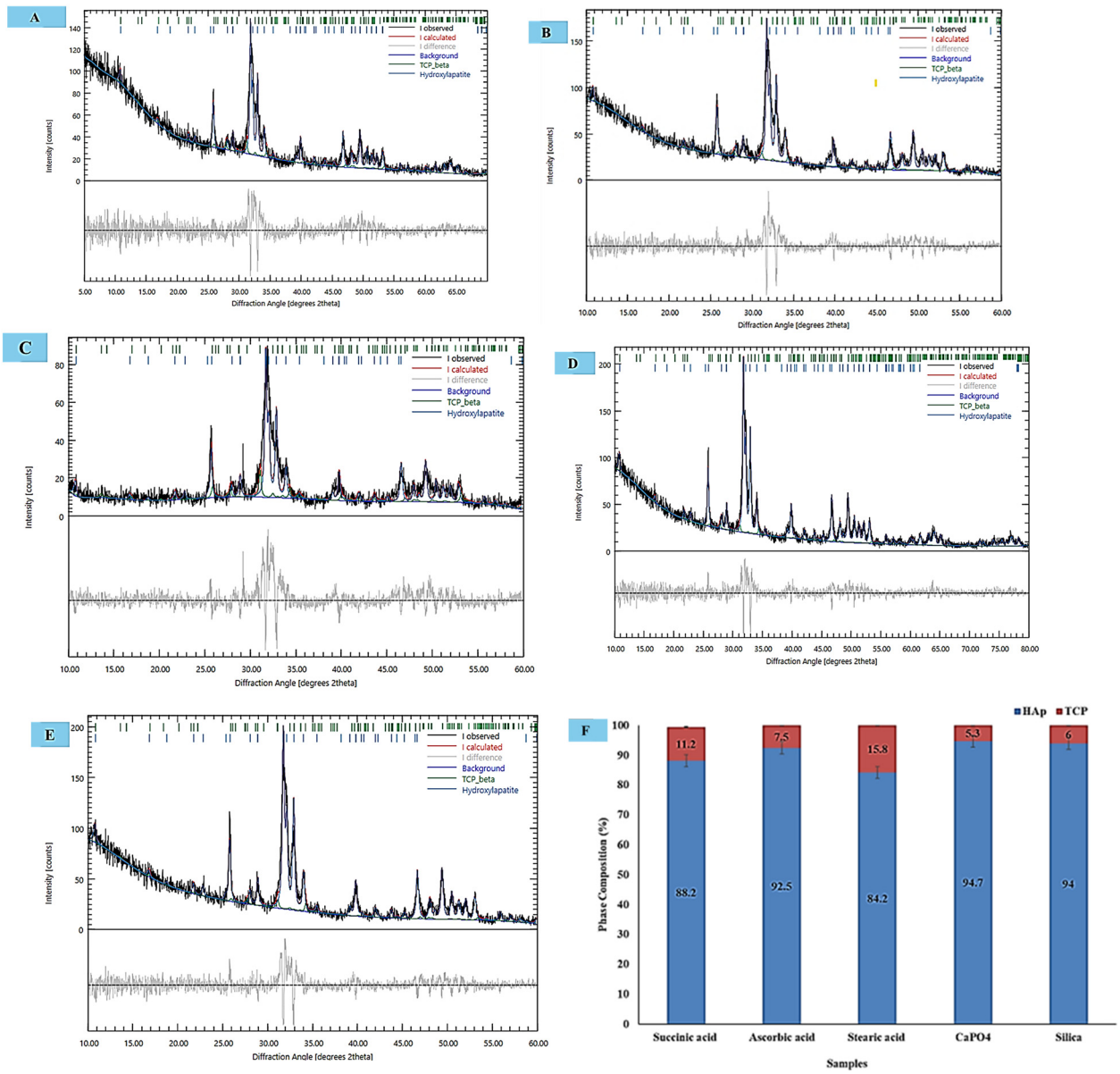

Fig. 13 Rietveld refinement and phase analysis results for (A) succinic acid_HAp (B) ascorbic acid_HAp, (C) stearic acid _HAp, (D) calcium phosphate_HAp, (E) silica_HAp and (F) phase composition.

4 Conclusion

This study investigated how the hydroxyapatite (HAp) structure changed under hydrothermal modification with organic modifiers (succinic acid, ascorbic acid, stearic acid) and inorganic modifiers (calcium phosphate, silica) by examining the crystallographic structure, morphology, and phase composition of HAp. The Williamson–Hall model measured crystallite sizes below 100 nm and microstructural parameters, showing stearic acid-modified HAp as having the largest crystallite size at 138.6 nm alongside a significant strain of 0.0167 and tensile stress of 100 093 N m^{-2}. Calcium phosphate modification yielded HAp with a minimum crystallite size of 0.148 nm but generated high compressive stress values reaching −83 187 N m^{-2}. In comparison, the succinic and ascorbic acid modifications achieved moderate crystallite sizes of 11.51 and 16.11 nm, respectively, making them suitable for biomedical use despite their varying strain and tensile stress measurements. SEM analysis showed that succinic acid-HAp developed bioactive clusters, whereas ascorbic acid-HAp took on a dispersible, fluffy form. Stearic acid-HAp formed mechanically stable rod-like structures, calcium phosphate-HAp demonstrated osteoconductive porosity, and silica-HAp presented layered flakes that allowed controlled drug delivery. The Rietveld refinement analysis showed that calcium phosphate-(94.7% HAp) and silica-modified HAp (94% HAp) possessed higher phase purity in contrast to stearic acid-HAp, which contained significant tricalcium phosphate impurities (15.8% TCP), leading to reduced refinement reliability (R_{wp}: highest for stearic acid-HAp). The results demonstrate that selecting appropriate modifiers determines the properties of HAp that are suitable for biomedical, mechanical, and energy applications.

Author contributions

Md. Kawsar synthesized and characterized the hydroxyapatites, executed the photocatalytic experiment, and wrote the draft and original manuscript. Md. Sahadat Hossain conceived and designed the experiment and analyzed the data. Dipa Islam conducted the SEM experiment. Newaz Mohammed Bahadur and Samina Ahmed supervised the findings of this work. Samina Ahmed supervised the overall work and managed the required facilities.

Data availability

Data will be made available upon request.

Conflicts of interest

No declaration of conflict is reported.

Acknowledgements

The authors are grateful to the Bangladesh Council of Scientific and Industrial Research (BCSIR) authority for financial support through the R&D project (ref. no. 39.02.0000.011.14.134.2021/900; Date: 30.12.2021). Md. Kawsar wishes to thank the Department of Applied Chemistry and Chemical Engineering, Noakhali Science and Technology University, Noakhali, Bangladesh, for approving the M. S. Thesis program.

References

1 A. Szcześ, L. Hołysz and E. Chibowski, Synthesis of hydroxyapatite for biomedical applications, *Adv. Colloid Interface Sci.*, 2017, **249**, 321–330.
2 D. F. Fitriyana, R. Ismail, Y. I. Santosa, S. Nugroho, A. J. Hakim and M. Syahreza Al Mulqi, Hydroxyapatite Synthesis from Clam Shell Using Hydrothermal Method: A Review 2019 International Biomedical Instrumentation and Technology Conference (IBITeC) 2019 International Biomedical Instrumentation and Technology Conference (IBITeC), 2019, vol. 1, pp. 7–11.
3 P. Szterner and M. Biernat, The Synthesis of Hydroxyapatite by Hydrothermal Process with Calcium Lactate Pentahydrate: The Effect of Reagent Concentrations, pH, Temperature, and Pressure, in *Bioinorganic Chemistry and Applications*, ed. G. Mendoza-Diaz, 2022, p. 3481677.
4 R. E. Riman, W. L. Suchanek, K. Byrappa, C.-W. Chen, P. Shuk and C. S. Oakes, Solution synthesis of hydroxyapatite designer particulates, *Solid State Ionics*, 2002, **151**, 393–402.
5 W. Suchanek and M. Yoshimura, Processing and properties of hydroxyapatite-based biomaterials for use as hard tissue replacement implants, *J. Mater. Res.*, 1998, **13**, 94–117.
6 L.-X. Yang, J.-J. Yin, L.-L. Wang, G.-X. Xing, P. Yin and Q.-W. Liu, Hydrothermal synthesis of hierarchical hydroxyapatite: preparation, growth mechanism and drug release property, *Ceram. Int.*, 2012, **38**, 495–502.
7 H. Nosrati, R. S. Mamoory, D. Q. S. Le and C. E. Bünger, Preparation of reduced graphene oxide/hydroxyapatite nanocomposite and evaluation of graphene sheets/hydroxyapatite interface, *Diamond Relat. Mater.*, 2019, **100**, 107561.
8 D. Smolen, T. Chudoba, I. Malka, A. Kedzierska, W. Lojkowski, W. Swieszkowski, K. J. Kurzydlowski, M. Kolodziejczyk-Mierzynska and M. Lewandowska-Szumiel, Highly biocompatible, nanocrystalline hydroxyapatite synthesized in a solvothermal process driven by high energy density microwave radiation, *IJN*, 2013, 653.
9 O. Sinitsyna, A. Veresov, E. Kovaleva, Y. V. Kolen'ko, V. Putlyaev and Y. Tretyakov, Synthesis of hydroxyapatite by hydrolysis of α-$Ca_3(PO_4)_2$, *Russ. Chem. Bull.*, 2005, **54**, 79–86.
10 H. Nosrati, R. S. Mamoory, D. Q. S. Le, C. E. Bünger, R. Z. Emameh and F. Dabir, Gas injection approach for synthesis of hydroxyapatite nanorods via hydrothermal method, *Mater. Charact.*, 2020, **159**, 110071.
11 X. Guo, H. Yan, S. Zhao, Z. Li, Y. Li and X. Liang, Effect of calcining temperature on particle size of hydroxyapatite synthesized by solid-state reaction at room temperature, *Adv. Powder Technol.*, 2013, **24**, 1034–1038.
12 M. Shirkhanzadeh, Direct formation of nanophase hydroxyapatite on cathodically polarized electrodes, *J. Mater. Sci.: Mater. Med.*, 1998, **9**, 67–72.

13 Md Kawsar, Md. S. Hossain, N. M. Bahadur and S. Ahmed, Synthesis of nano-crystallite hydroxyapatites in different media and a comparative study for estimation of crystallite size using Scherrer method, Halder–Wagner method size-strain plot, and Williamson–Hall model, *Heliyon*, 2024, **10**, e25347.
14 T. Zhang and X. Xiao, Hydrothermal Synthesis of Hydroxyapatite Assisted by Gemini Cationic Surfactant, *J. Nanomater.*, 2020, **2020**, 1–7.
15 G. Ma, Three common preparation methods of hydroxyapatite, *IOP Conf. Ser.: Mater. Sci. Eng.*, 2019, **688**, 033057.
16 S. Hussain and K. Sabiruddin, Effect of heat treatment on the synthesis of hydroxyapatite from Indian clam seashell by hydrothermal method, *Ceram. Int.*, 2021, **47**, 29660–29669.
17 Y. Yang, Q. Wu, M. Wang, J. Long, Z. Mao and X. Chen, Hydrothermal Synthesis of Hydroxyapatite with Different Morphologies: Influence of Supersaturation of the Reaction System, *Cryst. Growth Des.*, 2014, **14**, 4864–4871.
18 M. Jevtić, M. Mitrić, S. Škapin, B. Jančar, N. Ignjatović and D. Uskoković, Crystal Structure of Hydroxyapatite Nanorods Synthesized by Sonochemical Homogeneous Precipitation, *Cryst. Growth Des.*, 2008, **8**, 2217–2222.
19 R. Rial, M. González-Durruthy, Z. Liu and J. M. Ruso, Advanced Materials Based on Nanosized Hydroxyapatite, *Molecules*, 2021, **26**, 3190.
20 M. Kawsar, M. S. Hossain, S. Tabassum, D. Islam, N. Mohammed Bahadur and S. Ahmed, Crystal structure modification of nano-hydroxyapatite using organic modifiers and hydrothermal technique, *RSC Adv.*, 2024, **14**, 29665–29674.
21 M. A. Fanovich, M. S. Castro and J. M. P. López, Structural analysis of modified hydroxyapatite powders, *Mater. Res. Bull.*, 2001, **36**, 487–496.
22 H. Zhu, D. Guo, H. Zang, D. A. H. Hanaor, S. Yu, F. Schmidt and K. Xu, Enhancement of hydroxyapatite dissolution through structure modification by Krypton ion irradiation, *J. Mater. Sci. Technol.*, 2020, **38**, 148–158.
23 W. Guan, N. Hayashi, S. Ihara, S. Satoh, C. Yamabe, M. Goto, Y. Yamaguchi and A. Danjoh, Modification of Hydroxyapatite Crystallization Using IR Laser, *Free Electron Lasers 2003*, Elsevier, 2004, pp. II-75–II-76.
24 S. Hossain Md, S. M. Tuntun, N. M. Bahadur and S. Ahmed, Enhancement of photocatalytic efficacy by exploiting copper doping in nano-hydroxyapatite for degradation of Congo red dye, *RSC Adv.*, 2022, **12**, 34080–34094.
25 H. Zanin, E. Saito, F. R. Marciano, H. J. Ceragioli, A. E. C. Granato, M. Porcionatto and A. O. Lobo, Fast preparation of nano-hydroxyapatite/superhydrophilic reduced graphene oxide composites for bioactive applications, *J. Mater. Chem. B*, 2013, **1**, 4947–4955.
26 S. P. Muhoza, T. H. Taylor, X. Song and M. D. Gross, The Impact of Sintering Atmosphere and Temperature on the Phase Evolution of High Surface Area LSCF Prepared by In Situ Carbon Templating, *J. Electrochem. Soc.*, 2021, **168**, 034519.
27 S. Hossain Md, A. A. Shaikh Md, S. Rahaman Md and S. Ahmed, Modification of the crystallographic parameters in a biomaterial employing a series of gamma radiation doses, *Mol. Syst. Des. Eng.*, 2022, **7**, 1239–1248.
28 M. Bin Mobarak, S. Hossain Md, Z. Yeasmin, M. Mahmud, M. Rahman Md, S. Sultana, S. M. Masum and S. Ahmed, Probing the photocatalytic competency of hydroxyapatite synthesized by solid state and wet chemical precipitation method, *J. Mol. Struct.*, 2022, **1252**, 132142.
29 A. A. Akl and A. S. Hassanien, Microstructure and crystal imperfections of nanosized CdS Se^{1-} thermally evaporated thin films, *Superlattices Microstruct.*, 2015, **85**, 67–81.
30 A. A. Akl, S. A. Aly and M. A. Kaid, Microstructural and Electrical Properties of $(WO_3)_{1-x}(MoO_3)_x$ Thin Films Synthesized by Spray Pyrolysis Technique, *Research & Reviews: Journal of Material Sciences*, 2017, **1**, 10–19.
31 K. C. Vinoth Kumar, T. Jani Subha, K. G. Ahila, B. Ravindran, S. W. Chang, A. H. Mahmoud, O. B. Mohammed and M. A. Rathi, Spectral characterization of hydroxyapatite extracted from Black Sumatra and Fighting cock bone samples: a comparative analysis, *Saudi J. Biol. Sci.*, 2021, **28**, 840–846.
32 W. Tong, J. Chen, X. Li, J. Feng, Y. Cao, Z. Yang and X. Zhang, Preferred orientation of plasma sprayed hydroxyapatite coatings, *J. Mater. Sci.*, 1996, **31**, 3739–3742.
33 R. Stylianou, M. Tkadletz, N. Schalk, M. Penoy, C. Czettl and C. Mitterer, Effects of reference materials on texture coefficients determined for a CVD α-Al_2O_3 coating, *Surf. Coat. Technol.*, 2019, **359**, 314–322.
34 S. K. Sahoo, A. Madhuri, A. Saini, S. Jena, P. S. Devi, S. Laha and B. P. Swain, Correlation of microstructural and chemical bonding of FeNi-rGO nanocomposites, *J. Alloys Metallurgical Systems*, 2023, **4**, 100035.
35 S. Prosad Moulick, Md Sahadat Hossain, Md Zia Uddin Al Mamun, F. Jahan, Md Farid Ahmed, R. A. Sathee, Md Sujan Hossen, M. Ashraful Alam, Md Sha Alam and F. Islam, Characterization of waste fish bones (Heteropneustes fossilis and Otolithoides pama) for photocatalytic degradation of Congo red dye, *Results Eng.*, 2023, **20**, 101418.
36 R. Das and S. Sarkar, Determination of intrinsic strain in poly(vinylpyrrolidone)-capped silver nano-hexapod using X-ray diffraction technique, *Curr. Sci.*, 2015, **109**, 775–778.
37 B. Himabindu, N. S. M. P. Latha Devi, G. Sandhya, T. Naveen Reddy, T. Saha, B. Rajini Kanth and Md Sarowar Hossain, Structure based photocatalytic efficiency and optical properties of ZnO nanoparticles modified by annealing including Williamson–Hall microstructural investigation, *Mater. Sci. Eng., B*, 2023, **296**, 116666.
38 R. Jacob and J. Isac, X-ray diffraction line profile analysis of $Ba_{0.6}Sr_{0.4}Fe_xTi_{(1-x)}O_{3-\delta}$, ($x$ = 0.4), *Int. J. Chem. Stud.*, 2015, **2**, 12–21.
39 W. H. Hall, X-Ray Line Broadening in Metals, *Proc. Phys. Soc., London, Sect. A*, 1949, **62**, 741.
40 M. A. Tagliente and M. Massaro, Strain-driven (002) preferred orientation of ZnO nanoparticles in ion-implanted silica, *Nucl. Instrum. Methods Phys. Res., Sect. B*, 2008, **266**, 1055–1061.
41 S. Sarkar and R. Das, Determination of structural elements of synthesized silver nano-hexagon from X-ray diffraction analysis, *IJPAP*, 2018, **56**(10), 765–772.

42 M. Kawsar, M. S. Hossain, S. Tabassum, N. Mohammed Bahadur and S. Ahmed, Different solvents and organic modifiers for the control of crystallographic parameters in nano-crystallite hydroxyapatite for amplification of photocatalytic activity, *Nanoscale Adv.*, 2024, **6**, 2682–2700.
43 S. Nikmehr, M. Kazemzad, M. M. Sabzehmeidani, L. Nikzad, T. Ebadzadeh and M. Mousaei, Zn-based MOFs materials fabricated by mechanochemical ball milling and hydrothermal method and derived metal oxides, *Results Chem.*, 2023, **5**, 100973.
44 Md Sahadat Hossain and S. Ahmed, Sustainable synthesis of nano CuO from electronic waste (E-waste) cable: evaluation of crystallite size via Scherrer equation, Williamson–Hall plot, Halder–Wagner model, Monshi–Scherrer model, size-strain plot, *Results Eng.*, 2023, **20**, 101630.
45 A. Khorsand Zak, W. H. Abd. Majid, M. E. Abrishami and R. Yousefi, X-ray analysis of ZnO nanoparticles by Williamson–Hall and size–strain plot methods, *Solid State Sci.*, 2011, **13**, 251–256.
46 A. Hepp and C. Baerlocher, Learned Peak Shape Functions for Powder Diffraction Data, *Aust. J. Phys.*, 1988, **41**, 229–236.
47 L. Motevalizadeh, Z. Heidary and M. Ebrahimizadeh Abrishami, Facile template-free hydrothermal synthesis and microstrain measurement of ZnO nanorods, *Bull. Mater. Sci.*, 2014, **37**, 397–405.
48 N. C. Halder and C. N. J. Wagner, Separation of particle size and lattice strain in integral breadth measurements, *Acta Crystallogr.*, 1966, **20**, 312–313.
49 S. Hossain Md, M. Mahmud, M. B. Mobarak, S. Sultana, A. A. Shaikh Md and S. Ahmed, New analytical models for precise calculation of crystallite size: application to synthetic hydroxyapatite and natural eggshell crystalline materials, *Chem. Pap.*, 2022, **76**, 7245–7251.
50 U. Holzwarth and N. Gibson, The Scherrer equation versus the ''Debye-Scherrer equation'', *Nat. Nanotechnol.*, 2011, **6**, 534.
51 S. I. Yusuf, S. J. Mohammad and M. H. Ali, Scherrer andWilliamson-Hall estimated particle size using XRD analysis for cast aluminum alloys, *J. Theor. Appl. Phys.*, 2024, **18**, 012029.
52 M. E. Rodriguez-Garcia, S. M. Londoño-Restrepo, C. F. Ramirez-Gutierrez and B. Millan-Malo, *Effect of the crystal size on the X-ray diffraction patterns of isolated orthorhombic starches: a-type*, *Cornel University*, 2018, **https://arxiv.org/abs/1808.02966**.
53 S. Koutsopoulos, Synthesis and characterization of hydroxyapatite crystals: a review study on the analytical methods, *J. Biomed. Mater. Res.*, 2002, **62**, 600–612.
54 N. Kourkoumelis and M. Tzaphlidou, Spectroscopic Assessment of Normal Cortical Bone: Differences in Relation to Bone Site and Sex, *Sci. World J.*, 2010, **10**, 402–412.
55 N. K. Nguyen, M. Leoni, D. Maniglio and C. Migliaresi, Hydroxyapatite nanorods: soft-template synthesis, characterization and preliminary in vitro tests, *J. Biomater. Appl.*, 2013, **28**, 49–61.
56 R. A. Ramli, R. Adnan, M. Abu Bakar and S. Masudi, Synthesis and characterisation of pure nanoporous hydroxyapatite, *J. Phys. Sci.*, 2011, **22**, 25–37.
57 D. Davazoglou and V. Em Vamvakas, Arrangement of Si and O Atoms in Thermally Grown SiO[sub 2] Films, *J. Electrochem. Soc.*, 2003, **150**, F90.
58 C. Li, B. Zhao, Y. Lu and Y. Liang, Microstructure and Ion Exchange in Stearic Acid Langmuir–Blodgett Films Studied by Fourier Transform Infrared-Attenuated Total Reflection Spectroscopy, *J. Colloid Interface Sci.*, 2001, **235**, 59–65.
59 S. Raynaud, E. Champion, D. Bernache-Assollant and P. Thomas, Calcium phosphate apatites with variable Ca/P atomic ratio I. Synthesis, characterisation and thermal stability of powders, *Biomaterials*, 2002, **23**, 1065–1072.
60 M. Manzano and M. Vallet-Regí, New developments in ordered mesoporous materials for drug delivery, *J. Mater. Chem.*, 2010, **20**, 5593.
61 Md. S. Hossain, Md. A. A. Shaikh, Md. F. Ahmed and S. Ahmed, Synthesis and characterization of nanocrystallite triple superphosphate from waste *Pila globosa* shells for sustainable industrial production, *Mater. Adv.*, 2023, **4**, 2384–2391.
62 M. Kawsar, M. S. Hossain, S. Tabassum, N. M. Bahadur and S. Ahmed, Synthesis of different types of nano-hydroxyapatites for efficient photocatalytic degradation of textile dye (Congo red): a crystallographic characterization, *RSC Adv.*, 2024, **14**, 11570–11583.
63 S. Rehman, A. Mumtaz and S. K. Hasanain, Size effects on the magnetic and optical properties of CuO nanoparticles, *J. Nanopart. Res.*, 2011, **13**, 2497–2507.